Acta Pharmaceutica Sinica B 2025;15(1):592–610

Chinese Pharmaceutical Association
Institute of Materia Medica, Chinese Academy of Medical Sciences

Acta Pharmaceutica Sinica B

www.elsevier.com/locate/apsb
www.sciencedirect.com

ORIGINAL ARTICLE

Caffeic acid-vanadium nanozymes treat skin flap ischemia-reperfusion injury through macrophage reprogramming and the upregulation of X-linked inhibitors of apoptotic proteins

Xinyu Zhao[a,†], Jie Shan[a,†], Hanying Qian[a,b,†], Xu Jin[a,†], Yiwei Sun[c], Jianghao Xing[c], Qingrong Li[c], Xu-Lin Chen[a,*], Xianwen Wang[c,*]

[a]*Department of Burns, The First Affiliated Hospital of Anhui Medical University, Hefei 230022, China*
[b]*Department of Graduate School, Anhui University of Chinese Medicine, Hefei 230022, China*
[c]*School of Biomedical Engineering, Anhui Medical University, Hefei 230032, China*

Received 14 May 2024; received in revised form 20 August 2024; accepted 22 August 2024

KEY WORDS

Caffeic acid-vanadium;
Nanozymes;
Skin flap;
Ischemia-reperfusion;
Oxidative stress;
Inflammation;
Chemokines;
Apoptosis

Abstract Ischemia-reperfusion (I/R) injury following skin flap transplantation is a critical factor leading to flap necrosis and transplant failure. Antagonizing inflammatory responses and oxidative stress are regarded as crucial targets for mitigating reperfusion injury and enhancing flap survival. In this study, caffeic acid-vanadium metal polyphenol nanoparticles (CA-V NPs) were prepared for the treatment of skin flap ischemia and reperfusion. This study was conducted using a one-step method to prepare new types of CA-V NPs with uniform sizes and stable structures. *In vitro*, the CA-V NPs exhibited CAT-like and SOD-like activities and could effectively scavenge ROS, generate oxygen, and alleviate oxidative stress. In the H_2O_2-induced cellular oxidative stress model, CA-V NPs effectively reduced ROS levels and inhibited apoptosis through the XIAP/Caspase-3 pathway. In the cellular inflammation model induced by LPS combined with IFN-γ, CA-V NPs reprogrammed macrophage polarization toward the M2 phenotype and reduced inflammatory responses by reducing the expression of the chemokines CCL4 and CXCL2. In addition, animal experiments have shown that CA-V NPs can alleviate oxidative stress in skin flap tissues, inhibit apoptosis, promote angiogenesis, and ultimately improve the survival rate of skin flaps. CA-V NPs provide a new target and strategy for the treatment of flap I/R injury.

*Corresponding authors.
E-mail addresses: okcxl@126.com (Xu-Lin Chen), xianwenwang@ahmu.edu.cn (Xianwen Wang).
[†]These authors made equal contributions to this work.
Peer review under the responsibility of Chinese Pharmaceutical Association and Institute of Materia Medica, Chinese Academy of Medical Sciences.

https://doi.org/10.1016/j.apsb.2024.08.022

1. Introduction

Ischemia-reperfusion (I/R) injury after skin flap transplantation is an important cause of necrosis and graft failure[1]. The mechanism of I/R is complex, and I/R can cause phenotypic alterations in endothelial function, which include increased vascular permeability[2], increased expression of endothelial cell adhesion molecules, increased inflammatory mediators, impaired microcirculatory capillary function and microvascular occlusion, causing ischemia at the edges of the flap or overall[3]. At this stage, cell necrosis and apoptosis caused by oxidative stress, the inflammatory response, intracellular calcium overload, and leukocyte activation are considered to be important causes of I/R injury. The inflammatory response and oxidative stress are considered to be the main pathological aspects of tissue injury caused by I/R. Reactive oxygen species (ROS) and reactive nitrogen species (RNS) are the main causes of oxidative reactions in biomolecules. Low concentrations of ROS play important roles in regulating cellular functions[4]. However, excessive ROS often leads to oxidative stress, damage to cellular lipids, proteins, and DNA, and the induction of apoptosis and necrosis[5,6]. During the ischemic phase, the skin flap is unable to obtain sufficient oxygen and nutrients due to the interruption of the blood supply, and the cells produce ROS and RNS, which gradually accumulate, leading to the onset of oxidative stress. During the reperfusion phase, oxygen is reinjected into tissue subjected to ischemia, leading to a dramatic increase in ROS and the activation of multiple cell signaling pathways and biomolecules[7]. However, an excessive inflammatory response leads to a localized state of hyperreactivity in the skin flap. During the ischemic phase, immune cells release a variety of cytokines and inflammatory mediators, such as interleukin (IL) and tumor necrosis factor (TNF-α), which activate the immune system[8]. During the reperfusion phase, a variety of chemokines, such as those in the CXC and CC families, are released, which further promotes the activation and aggregation of various inflammatory cells, as well as the activation of proinflammatory M1 macrophages, which enhances the inflammatory response and ultimately exacerbates cellular damage and the spread of inflammation. Therefore, antagonizing the inflammatory response and oxidative stress is regarded as an important target for attenuating reperfusion injury and improving flap survival.

The inhibitor of apoptosis protein (IAP) family is a highly conserved family of endogenous antiapoptotic factors that mainly inhibit cell apoptosis by suppressing caspase activity and participating in the regulation of nuclear factor-kappa B (NF-κB). X-linked inhibitor of apoptosis protein (XIAP) is a recently discovered major member of the IAP family and is the strongest apoptosis inhibitor in the IAP family. It primarily inhibits the activity of executioner caspases (such as Caspase-3 and Caspase-7) and initiator caspases (such as Caspase-9) by binding to and inhibiting them. On the other hand, the expression of various cell chemotactic factors, such as CXC and CC, promotes the occurrence of inflammation in I/R. Among them, C−C motif chemokine ligand 4 (CCL4) and chemokine C−X−C motif ligand 2 (CXCL2) are important regulatory factors secreted by macrophages. CCL4 and CXCL2 can attract and guide macrophages toward inflammatory sites or damaged tissues, stimulate the synthesis and release of inflammatory mediators (such as TNF-α, IL-1β, and IL-6), promote macrophage expression of the M1 phenotype, and exacerbate the inflammatory response. By downregulating the NF-κB pathway, targeting the XIAP protein, and downregulating the expression of CCL4 and CXCL2, the NF-κB pathway can serve as a new therapeutic target for I/R.

In recent years, nanomaterials have been widely used in the information industry, environmental engineering, and biomedicine[9-13]. Nanozymes are enzyme-active nanomaterials that regulate ROS levels in organisms[14-16]. Superoxide dismutase (SOD) and catalase (CAT) are antioxidant enzymes that protect cells from free radicals[17-19]. SOD enzymes catalyze the disproportionation of superoxide anion radicals ($O_2^{\cdot -}$) to produce O_2 and H_2O_2[20,21]. CAT enzymes decompose hydrogen peroxide to produce oxygen[22]. The combined use of SOD and CAT can effectively reduce oxidative stress and promote tissue repair[23]. Metallic nanomaterials often possess multiple types of enzymatic activities, making them ideal alternatives to natural enzymes[24-26]. Vanadium (V) is an essential metal element in the human body that plays an important role in the metabolism of cholesterol and triglycerides, as well as in the oxidation of glucose and the synthesis of glycogen[27,28]. Several studies at this stage have shown that metal polyphenol nanomaterials prepared by combining metal elements with natural antioxidant products can significantly improve antioxidant and anti-inflammatory capacity. Caffeic acid (CA) is a natural polyphenolic compound extracted from coffee, and its aromatic core, conjugated double bonds, and hydroxyl groups give it excellent antioxidant properties[29,30]. The o-diphenol hydroxyl group in CA can provide hydrogen atoms or electrons to stabilize free radicals, forming semiquinone radicals and ultimately CA *O*-quinone derivatives, thus scavenging free radicals; at the same time, CA can chelate metal elements with its two hydroxyl groups, reducing the formation of free radicals. CA can effectively improve the intracellular redox status, reduce NF-κB signaling, reduce ROS production, downregulate the inflammatory response, and inhibit apoptosis[31-34]. CA plays an important role in the treatment of diabetes mellitus, atherosclerosis, Alzheimer's disease, inflammatory bowel disease, and other diseases[35-39]. Additionally, CA derivatives have a wide range of applications in antitumor and antimicrobial therapies, but no studies have reported their application in I/R therapy[40-43].

Coordinating metal elements with natural antioxidants and exploring metal polyphenol nanomaterials with superior antioxidant performance and various enzyme activities for I/R treatment have broad clinical application value. In this study, novel caffeic acid-vanadium metal polyphenol nanoparticles (CA-V NPs), which can clear reactive oxygen species and regulate various biological processes during the I/R of skin flaps, were prepared to promote flap survival (Fig. 1). CA-V NPs with a uniform size and stable structure were prepared by one-step coordination of the metal element V with the natural product CA. Among them, CA-V NPs have CAT-like and SOD-like activities and can reduce inflammatory responses and protect cells from oxidative damage by scavenging ROS and providing O_2. In an H_2O_2-induced

oxidative stress model, CA-V NPs effectively lowered ROS levels and inhibited cell apoptosis through the XIAP/Caspase-3 pathway. In a model of inflammation induced by lipopolysaccharide (LPS) combined with interferon-γ (IFN-γ), CA-V NPs downregulated various inflammatory pathways, reduced the expression of chemotactic factors such as CCL4 and CXCL2, reprogrammed macrophages toward the M2 phenotype, and decreased the inflammatory response. The sequencing results of the two cell models showed that genes associated with oxidative stress, the inflammatory response, and apoptosis that were significantly downregulated in both groups of models after treatment with CA-V NPs were enriched in the TNF-α, JAK-STAT, IL-17, and NF-κB signaling pathways. In addition, animal experiments have shown that CA-V NPs can alleviate oxidative stress in skin flap tissues, inhibit apoptosis, promote angiogenesis, and ultimately improve the survival rate of skin flaps. Moreover, the CA-VNPs showed good biological safety. CA-V NPs, which are multi-catalytically active nanozymes, provide a new target and strategy for the treatment of flap I/R injury.

2. Materials and methods

2.1. Materials

NH_4VO_3 (7803-55-6), caffeic acid (142039-77-8), 2,2′-azinobis-(3-ethylbenzothiazoline-6-sulfonate) (ABTS) (30931-67-0), 2,2-

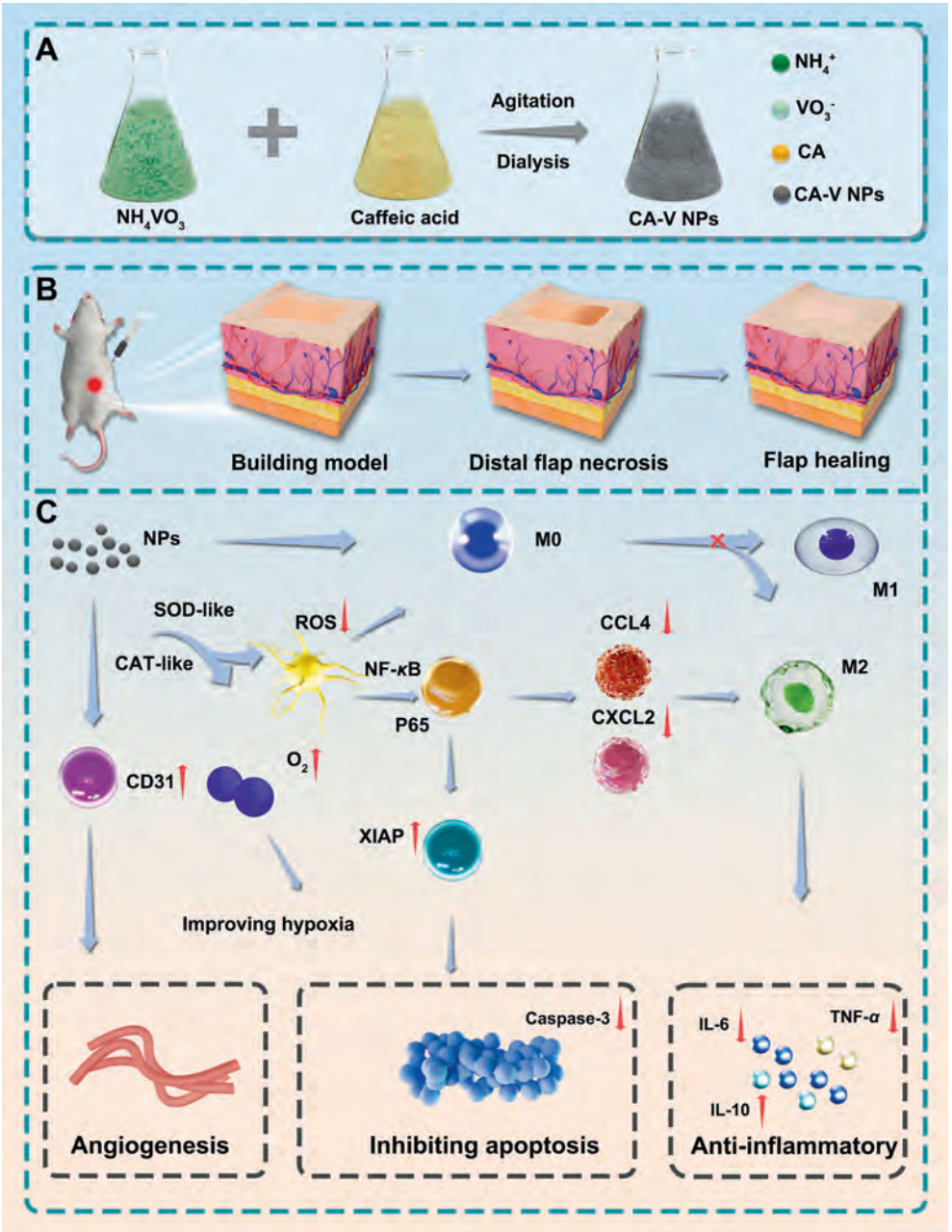

Figure 1 (A) Schematic diagram of CA-V NP synthesis; (B) Schematic diagram of CA-V NPs promoting flap healing. (C) Diagram of the mechanism by which CA-V NPs promote flap I/R repair.

diphenyl-L-picrylhydrazyl (DPPH) (1898-66-4) (Chongqing, China, Macklin Biochemical Co., Ltd.); H_2O_2 (7722-84-1) (Sichuan, China, XiLong Scientific Co., Ltd.); LPS (SJ-MB0005), and Cell Counting Kit-8 (CCK-8) (CT0001-B) (Shandong Sparkjade Biotechnology Co., Ltd.); apoptosis assay kit (BB-4101), cell viability assay kit (BB-4126) (Shanghai, China, Bestbio Co., Ltd.); SOD assay kit (S0101-3); ROS assay kit (S0033M), NO assay kit (S0019) (Shanghai, China, Beyotime Co., Ltd.); inducible nitric oxide synthase (iNOS) antibody (AF0199), CXCL2 (DF12551) antibodies for Western blotting (WB), and XIAP (AF6368), Caspase-3 (AF7022) antibodies for immunohistochemistry (IH) (Changzhou, China, Affinity Co., Ltd.); CD206 antibody (60143-1-Ig) (Wuhan, China, Proteintech Co., Ltd.); enzyme-linked immunosorbent assay (ELISA) kits for IL-6 (JL20268), IL-10 (JL20242), TNF-α (JL10484) (Shanghai, China, Jianglai Biology Co., Ltd.); IFN-γ (PD201231), P65 (380172), P-P65 (310013), XIAP (R26117), Caspase-3 (R23727), CCL4 (R389145) antibodies for WB (Chengdu, China, Zenbio Co., Ltd.); *XIAP*, *Caspase-3*, *Ccl4*, and *Cxcl2* for real-time quantitative polymerase chain reaction (qPCR) primers (Chuzhou, China, General Biol Co., Ltd.); and CD31 (GB113151), CD68 (GB113109) antibodies for IH (Wuhan, China, Servicebio Co., Ltd.). CCL4 (bs-1046R), and CXCL2 (bs-20208R) antibodies for IH (Beijing, China, Bioss Co., Ltd.).

2.2. Synthesis of CA-V NPs

CA-V NPs were prepared using a one-step self-assembly method. First, 234 mg of NH_4VO_3 was dissolved in 20 mL of deionized water and stirred for 15 min. Then, 360.3 mg of CA was dissolved in 20 mL of deionized water, slowly added to the NH_4VO_3 solution, and vigorously stirred for 12 h. The reaction mixture was placed in a dialysis bag with a molecular weight cutoff of 8000−14,000 and dialyzed for 24 h to prepare CA-V NPs.

2.3. Characterization of CA-V NPs

The V content in the samples was quantified *via* inductively coupled plasma−optical emission spectrometry (ICP−OES) (Puyu Technology, EXPEC 6500, Hangzhou, China); the morphological features of the CA-V NPs were observed *via* transmission electron microscopy (TEM) (Thermo Scientific, Talos L120C G2, Beijing, China); the functional groups of the CA-V NPs were determined *via* Fourier transform infrared spectroscopy (FTIR) (Yingsa Optics, FOLI20, Shanghai, China); the elemental composition, chemical states, and chemical bond distribution of the CA-V NPs were investigated *via* X-ray photoelectron spectroscopy (XPS) (Thermo Scientific, K-Alpha, Beijing, China); the crystal structure of the CA-V NPs was examined *via* X-ray diffraction (XRD) (Bruker, D8 ADVANCE, Beijing, China); and the zeta potential and hydration particle size of the CA-V NPs were measured *via* a zeta potential analyzer (NanoBrook, 90Plus PALS, Shanghai, China).

2.4. Cell culture

In this study, human umbilical vein endothelial cells (HUVECs), mouse fibroblasts (L929 cells), and mouse macrophages (RAW 264.7 cells) from three different sources were used for *in vitro* experiments. HUVECs and L929 cells were cultured in DMEM supplemented with 10% fetal bovine serum, 100 U/mL penicillin, and 100 U/mL streptomycin. RAW 264.7 cells were cultured in a macrophage-specific culture medium. All cells were cultured in a CO_2 incubator at 37 °C with 5% carbon dioxide. The culture medium and cell passage were changed according to the cell growth status.

2.5. Scratch assay

L929 cells were seeded in a 6-well plate, and a uniform line of similar width was scratched in the center of the well. After the cells were washed with PBS three times to remove cell debris, a serum-free culture medium containing different concentrations of CA-V (0, 10, or 20 μg/mL) was added to each well. The growth of cells at the scratch was recorded using a microscope imaging system (Cole−Parmer, Motic Instruments AE2000, Shanghai, China) at 0, 24, 48, and 72 h to assess cell migration.

2.6. H_2O_2-induced oxidative stress damage in HUVECs

HUVECs were treated with a serum-free culture medium containing 1 mmol/L H_2O_2 for 1 h to induce oxidative stress. Different concentrations of CA-V was added, and the cells were coincubated for 4 h. The CCK-8 assay was used to detect the survival of HUVECs. NO and ROS staining kits were used for staining, and the staining conditions were observed under a confocal laser scanning microscope (Zeiss, LSM800, Beijing, China). Flow cytometry (Beckman Coulter, CytoFLEX, Shanghai, China) was used to determine the flow cytometry count of the HUVECs.

2.7. LPS in combination with IFN-γ induces the RAW 264.7 inflammatory response

RAW 264.7 cells were seeded in a 6-well plate and treated with 100 ng/mL LPS and 20 ng/L IFN-γ for 12 h to induce phenotypic changes and the secretion of related cytokines. Simultaneously, different concentrations of CA-V were added to the medium, and coincubation was performed for 12 h. Immunofluorescence staining for the M1/M2-related markers INOS/CD206 was performed, and flow cytometry was used to determine the flow cytometry count of M1/M2 cells. ELISA kits were used to detect inflammatory factors and anti-inflammatory factors produced during this process.

2.8. Cell viability staining and apoptosis detection

HUVECs were uniformly seeded in a 6-well plate. After cell adhesion, 2 mmol/L H_2O_2 was added to each well, and the cells were incubated. Serum-free culture medium containing different concentrations of CA-V (0, 25, or 50 μg/mL) was added, and the cells were coincubated. Cell viability was assessed using cell viability staining kit, and cell apoptosis was detected using a dual-staining cell apoptosis detection kit. Flow cytometry was used to detect the number of apoptotic cells.

2.9. Animal experimental groups

Eight-week-old female BALB/c mice were selected as experimental animals. All animal experiments were reviewed and approved by the Animal Care and Use Committee of Anhui Medical University (No. LLSC20220731). The mice were randomly divided into four groups, each consisting of 6 mice: the Flap group (control group), Flap I/R group, saline treatment group

(saline group), and CA-V NP treatment group (CA-V group). In the Flap group, only flap separation was performed without vascular occlusion. The remaining three groups underwent flap separation and vascular occlusion. The control group and I/R group received no treatment. The saline group and CA-V group were pretreated before flap establishment, and 50 μL of saline or CA-V NPs (1 mg/mL) was subcutaneously injected into the central area of the flap. The flap model was established 1 h later, and the flap survival status was observed and recorded.

2.10. Construction of the flap animal model

Anesthesia was induced by intraperitoneal injection of 1% sodium pentobarbital at a dose of 50 mg/kg based on body weight. After anesthesia, the depilated mice were fixed in the supine position on a disinfected cloth. Using the midline of the mouse as the axis and the lower edge of the xiphoid as the upper end of the flap, a symmetrical pedicle flap was designed on both sides, with a flap size of approximately 1 cm × 2 cm. A microvascular clamp was used to occlude the pedicle of the flap (mainly occluding the superficial epigastric vessels) to block blood vessels in the flap. After 6 h[44], the microvascular clamp was removed, and the flap was sutured *in situ* with a 6−0 silk thread to establish a mouse flap I/R abdominal model (Supporting Information Fig. S1).

2.11. Flap blood flow assessment

Blood flow in the flaps of the mice in each group on Day 7 was evaluated using the laser speckle technique (Xunwei Optoelectronics, SIM BFI-HR PRO, Wuhan, China) and color Doppler blood flow imaging (CDFI) (FayiNuo, VINNO 6LAB, Beijing, China). Laser speckle technique: The laser probe was placed at the upper part of the flap area at a fixed height, and the entire flap area was set as the observation range. After measuring the skin blood perfusion in the set area, the imaging system automatically determined the skin blood perfusion data at different positions within the set range through the use of different color images. Color Doppler blood flow imaging: The probe was coated with a thick layer of ultrasound coupling agent, ensuring that the flap and the probe were fixed at a constant distance. The blood flow model was selected, and the probe was gently moved to record the blood flow in the flap area.

2.12. Statistical analysis

Statistical analysis was performed on the data from each experimental group. The numerical data are expressed as the mean ± standard deviation (SD). Nonpaired *t*-tests were used to compare the data between groups to determine whether there were significant differences. A significance level of $P < 0.05$ indicated statistical significance ($^{*}P < 0.05$, $^{**}P < 0.01$, $^{***}P < 0.005$, and $^{****}P < 0.001$).

3. Results and discussion

3.1. Synthesis and characterization of CA-V NPs

In this study, a one-step self-assembly method was employed to synthesize structurally stable and uniformly sized ultrasmall CA-V NP metal polyphenol nanoparticles using NH_4VO_3 and CA as the raw materials (Fig. 2A). When CA solution was added to the V metal solution, the transparent V solution immediately turned black, indicating a vigorous chemical reaction between the two substances and the formation of a new substance referred to as CA-V NPs. The structure and physical properties of this new substance were characterized by various detection methods. TEM revealed that the CA-V NPs had a uniform structure and were small in size (Fig. 2B, Supporting Information Fig. S2). The diameter of the CA-V NPs ranged between 3.28 nm and 5.64 nm, with an average diameter of 4.27 nm, as determined by Image J software (National Institutes of Health) (Fig. 2C). These results are similar to the dynamic light scattering (DLS) results (Supporting Information Fig. S3). The zeta potential of the CA-V NPs ranged from 5.28 to 5.48 mV (Fig. 2D). XPS was used to analyze the chemical composition and electronic structure of the CA-V NPs (Fig. 2E). The O1 peaks at 531.12, 532.22, and 533.12 eV were attributed to V-O, C=O, and C-O, respectively (Fig. 2F). Peaks at 531, 516, 401, and 284 eV indicated the presence of O 1s, V 2p, N 1s, and C 1sorbitals, confirming the successful coordination of CA and V, respectively. The V 2p spectrum was further divided into V^{4+} $2p_{3/2}$, V^{3+} $2p_{3/2}$, V^{4+} $2p_{1/2}$, and V^{3+} $2p_{1/2}$ at 516.32, 517.32, 523.42, and 524.62 eV, respectively (Fig. 2G). These results indicated that CA reduced V^{5+} with oxidative properties in NH_4VO_3 to V^{4+} and V^{3+}. XRD showed that the CA-V NPs were amorphous (Fig. 2H). According to the FTIR spectrum of the CA-V NPs, the double peaks at 3414 and 3178 cm^{-1} are attributed to the −OH stretching vibration peaks in the hydroxyl and carboxyl groups on the benzene ring, respectively. The 1628 cm^{-1} peak is attributed to C=O stretching vibrations. The peaks at 1500 and 1441 cm^{-1} are attributed to the vibrations of the C=C skeleton on the benzene ring. The 1271 and 1205 cm^{-1} peaks are attributed to C-OH stretching vibrations. The decreases in the intensities of the characteristic hydroxyl group peaks at 3414 and 3178 cm^{-1} suggested that the hydroxyl group may be coordinated with V. The peak at 1617 cm^{-1} was a C=C telescopic vibration peak. The peak at 1397 cm^{-1} is the −COO telescopic vibration peak. The peaks at 1199 and 1084 cm^{-1} are attributed to C-O telescopic vibrations. The 963 cm^{-1} peak is attributed to the =C-H out-of-plane swinging vibration. The new characteristic peaks at 815 cm^{-1} and 760 cm^{-1} are attributed to the V-O antisymmetric stretching vibration and symmetric stretching vibration peaks, respectively, which confirm the coordination between hydroxyl groups and V ions (Fig. 2I). *In Vitro* stability experiments revealed that CA-V NPs dissolved in different solutions caused no particle precipitation or color change on Day 7, confirming their stable preservation at room temperature (Fig. 2J). On Day 7, DLS analysis of CA-V NPs dispersed in different solvents revealed that the hydrated particle size of the CA-V NPs was almost unchanged (Supporting Information Fig. S4). This also proves the stability of CA-V NPs at room temperature.

3.2. Antioxidant capacity and enzyme-like activity of CA-V NPs

Free radical scavenging and enzyme-like activity detection experiments effectively reflect the antioxidant properties of nanomaterials. Fig. 3A shows the principles of CA-V NPs scavenging ABTS+ free radicals and DPPH free radicals, as well as the working principles of CAT and SOD enzymes. ABTS+ and DPPH free radical scavenging experiments were used to systematically assess the ability of CA-V NPs to scavenge free radicals. Potassium persulfate can oxidize ABTS diammonium

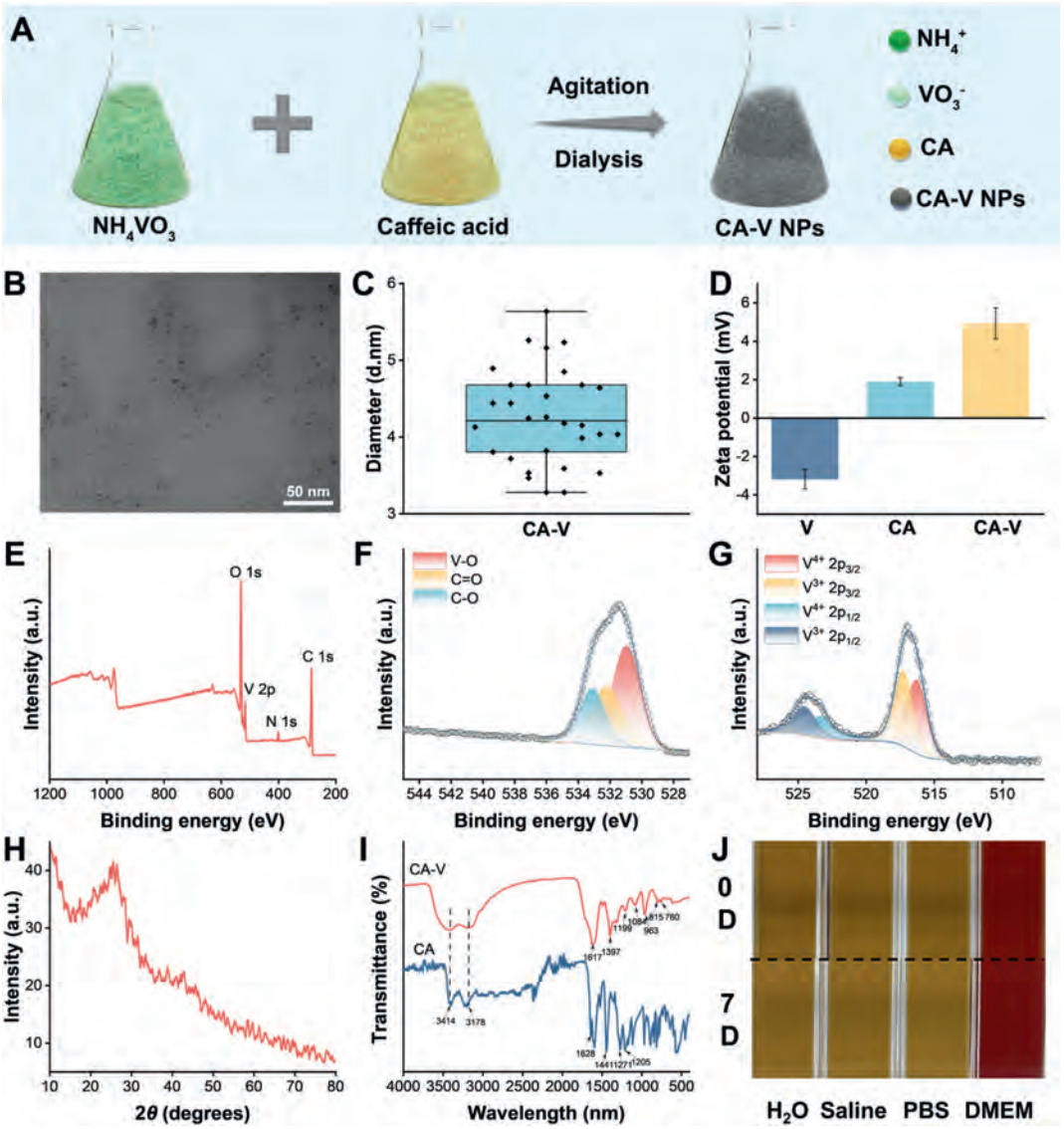

Figure 2 Preparation and characterization of CA-V NPs. (A) Schematic of the synthesis of CA-V NP. (B) TEM images of CA-V NPs (scale bar = 50 nm). (C) Particle size distribution of CA-V NPs. (D) Zeta potential of CA-V NPs. (E) Full-spectrum XPS spectrum of CA-V NPs. (F) XPS spectra of O 1s orbitals. (G) XPS spectrum of the V 2p orbital. (H) XRD patterns of CA-V NPs. (I) FTIR spectra of CA-V NPs. (J) Stability experiments of CA-V NPs. Data are presented as mean ± SD (n = 3).

salt solution into a blue ABTS+ solution, and the addition of antioxidants can effectively neutralize the oxidative capacity of ABTS+, reducing the maximum absorption wavelength (734 nm) of the ultraviolet absorption peak and causing the solution to fade or lighten in color. After CA-V NPs were added to the ABTS+ working solution, the mixture gradually became colorless, and this scavenging effect significantly increased with increasing concentrations of CA-V NPs (Fig. 3B). When the V concentration reached 0.4 μg/mL, the absorption peak at 734 nm decreased from 0.68 to 0.02, and almost all the ABTS+ free radicals were scavenged. The scavenging rate of ABTS+ was calculated through multiple experiments, and it was found that when the V concentration was 0.4 μg/mL, the scavenging rate reached 96.83% (Fig. 3E). The DPPH free radical solution appeared purple, and the added antioxidants could capture the unpaired electrons of the DPPH free radicals, reducing or eliminating their color. The experimental results showed that the addition of CA-V NPs efficiently reduced the characteristic absorption peak at 519 nm, eliminating the purple color of the solution (Fig. 3C). Moreover, this scavenging efficiency showed a certain concentration dependence. When the V concentration increased from 5 to 20 μg/mL, the DPPH concentration almost completely decreased, and the scavenging rate increased from 34.87% to 82.13% (Fig. 3F).

SOD and CAT are important antioxidants in the human body. Specifically, SOD enzymes can convert $O_2^{\cdot -}$ into H_2O_2 and O_2. Electron spin resonance spectroscopy (ESR) was used to detect the SOD-like activity of the CA-V NPs, and it was found that the CA-V NPs exhibited excellent $O_2^{\cdot -}$ scavenging ability (Fig. 3D). Additionally, the rate of $O_2^{\cdot -}$ scavenging by CA-V NPs was measured using a SOD assay kit. As the V concentration increased from 0 to 30 μg/mL, the $O_2^{\cdot -}$ scavenging rate

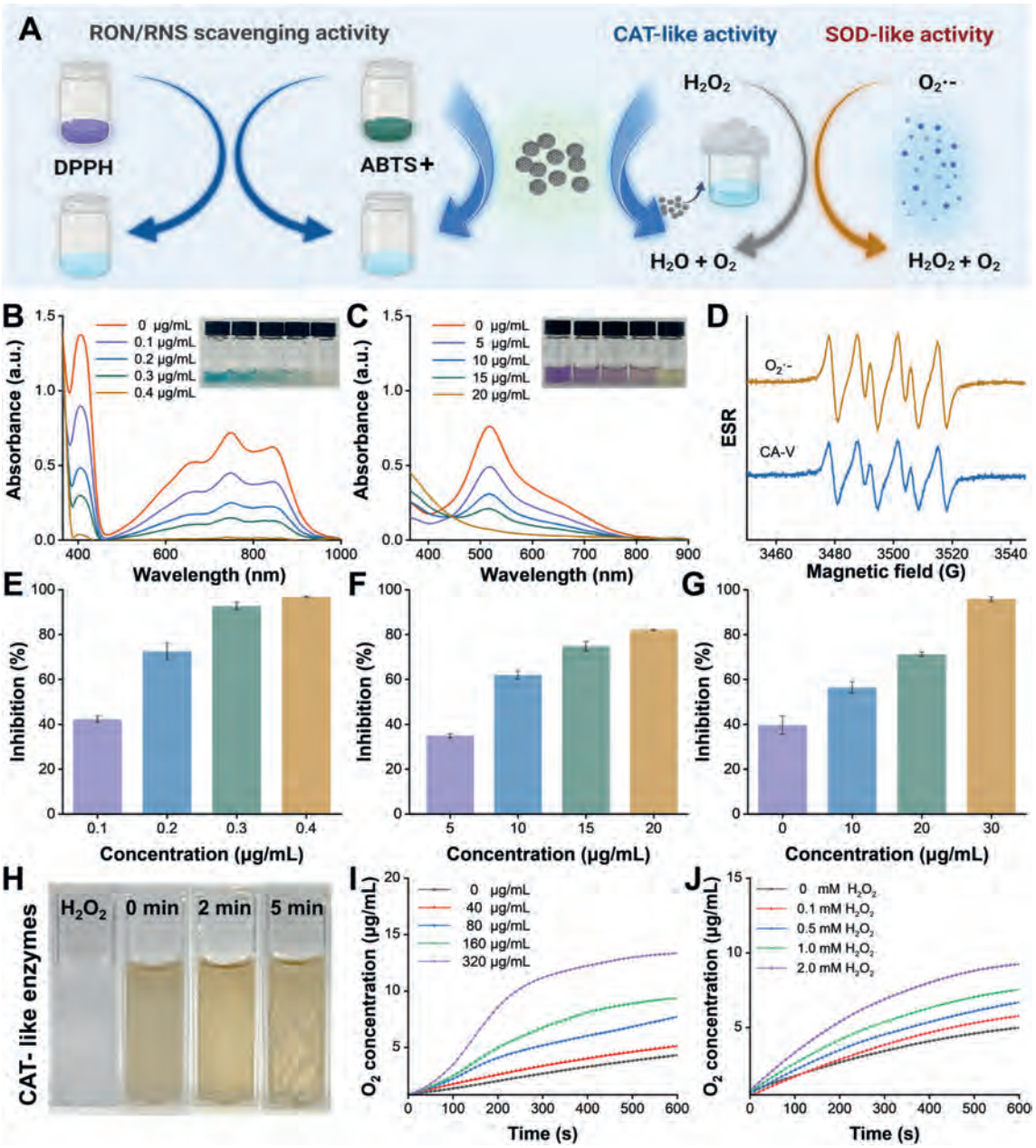

Figure 3 *In vitro* free radical scavenging capacity and enzyme-like activity of CA-V NPs. (A) Schematic diagram of the free radical scavenging and enzyme-like activity of CA-V NPs *in vitro*. (B, C) UV absorbance curves of CA-V NPs scavenging ABTS+ radicals and DPPH radicals. (D) ESR assay of the $O_2^{\cdot -}$ scavenging ability of CA-V NPs. (E-F) Rate of ABTS+ and DPPH radical scavenging by CA-V NPs. (G) Rate of $O_2^{\cdot -}$ scavenging by CA-V NPs. (H) Digital photographs of H_2O_2 decomposition by CA-V NPs. (I) O_2 release curves of CA-V NPs at different concentrations in H_2O_2 solution. (J) O_2 release curves of CA-V NPs in H_2O_2 solutions at different concentrations. Data are presented as mean ± SD ($n = 3$).

increased from 39.61% to 95.87% (Fig. 3G). The enzyme CAT is another antioxidant in the body that can decompose H_2O_2 into H_2O and O_2. After CA-V NPs were added to an H_2O_2 solution, bubbles were observed in the solution after 2 min, and the volume of the bubbles increased significantly after 5 min, confirming the CAT-like activity of the CA-V NPs (Fig. 3H). When different concentrations of CA-V NPs were added to the H_2O_2 solution, as the V concentration increased, the rate and total amount of O_2 released into the solution increased significantly (Fig. 3I). Subsequently, as the concentration of H_2O_2 increased, the reaction rate also increased (Fig. 3J). This indicates that the catalytic rate is positively correlated with the concentrations of CA-V NPs and H_2O_2.

3.3. *CA-V NPs protect cells from oxidative stress in vitro*

Before understanding the protective effect of CA-V NPs on cellular oxidative stress, the biocompatibility of CA-V NPs was assessed through cell toxicity and hemolysis experiments using a CCK-8 assay. After coculturing HUVECs, RAW 264.7 cells, and CA-V NPs, the viability of the HUVECs remained 100% when the V concentration reached 100 μg/mL (Fig. 4A). At a V

concentration of 150 μg/mL, the viability of the RAW 264.7 cells was approximately 92% (Fig. 4B). Cell hemolysis experiments are important research methods for studying the safety of materials in the body. In this study, when the V concentration reached 100 μg/mL, the red blood cells did not undergo hemolysis (Supporting Information Fig. S5). Both experiments demonstrated the good biocompatibility of CA-V NPs at low doses.

To evaluate the antioxidant capacity of CA-V NPs, H_2O_2-induced HUVEC models were constructed. In this model, the cell viability of the group treated with H_2O_2 alone was 59.87%, which was significantly lower than that of the CA-V NP treatment group (Fig. 4C). Moreover, with increasing concentrations of CA-V NPs, the cell viability approached that of the normal group. Fluorescence staining of cells stimulated with H_2O_2 using ROS and NO cell staining reagents and DAPI labeling of the cell nucleus revealed that ROS and NO exhibited green fluorescence, while the cell nucleus exhibited blue fluorescence. Confocal microscopic observation of the protective effect of CA-V NPs on cells revealed no obvious ROS or NO fluorescence signals in unstimulated cells, whereas cells stimulated with H_2O_2 exhibited abundant green fluorescence (Fig. 4D). As the concentration of CA-V NPs increased, the ROS and NO fluorescence gradually decreased and almost

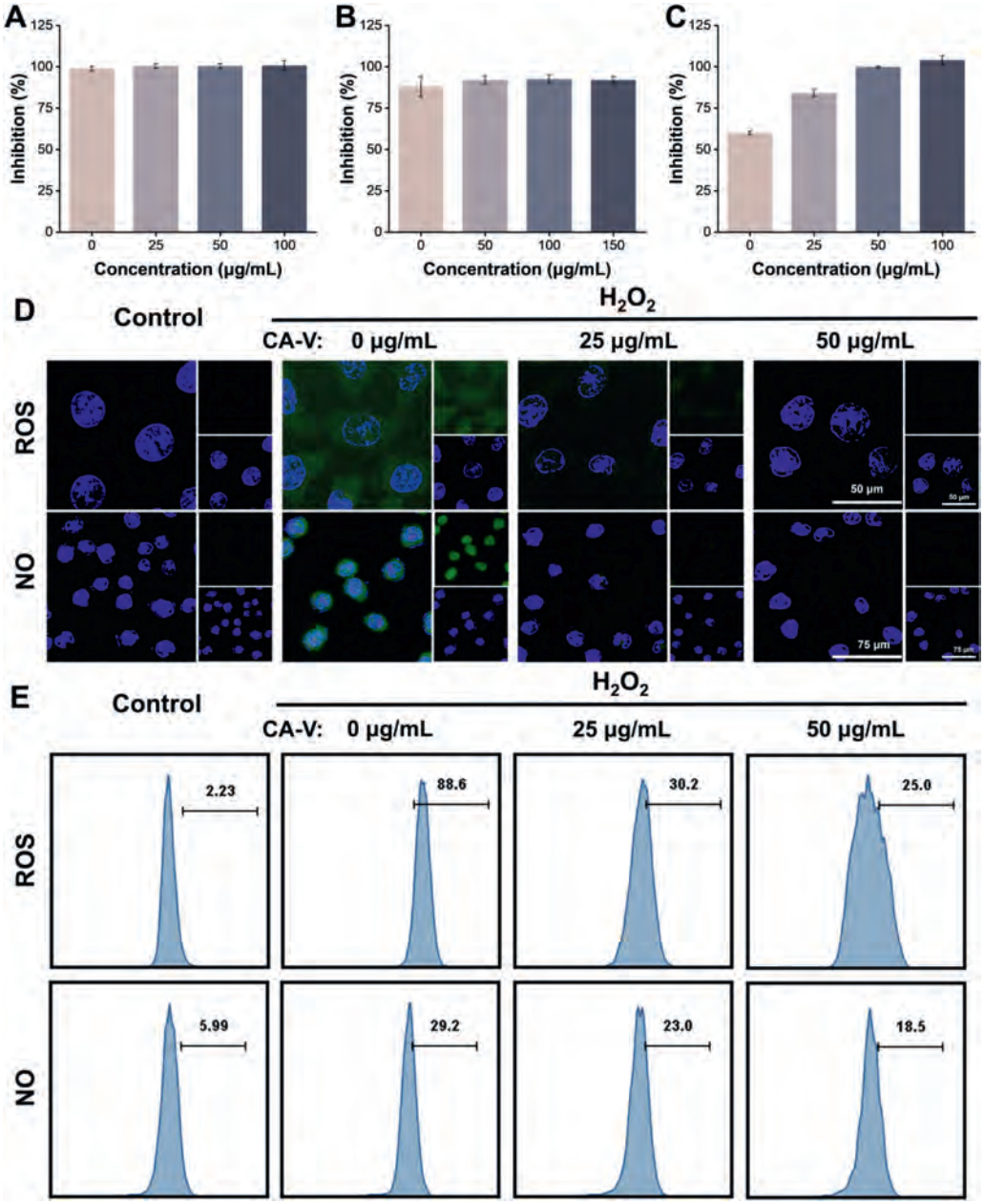

Figure 4 Biocompatibility and RONS scavenging ability of CA-V NPs *in vitro*. (A, B) The cytotoxicity of CA-V NPs to HUVECs, RAW 264.7 cells, was detected by a CCK-8 assay. (C) CCK-8 assay shows that CA-V NPs protect HUVECs from H_2O_2-induced oxidative damage. (D) Confocal fluorescence images of ROS and NO levels in HUVECs (ROS: scale bar = 50 μm. NO: scale bar = 75 μm). (E) Flow cytometry detection of ROS and NO levels in HUVECs. Data are presented as mean ± SD (n = 3).

completely disappeared at a concentration of 50 μg/mL, indicating that there was a positive correlation between the concentration of CA-V NPs and the efficiency of ROS and NO clearance. Flow cytometry confirmed these results (Fig. 4E). These results indicate that CA-V NPs can protect cells from H_2O_2-induced cellular damage.

3.4. CA-V NPs promote cell migration and inhibit apoptosis in vitro

Cell migration plays a crucial role in tissue repair. After coculturing L929 cells with the materials for 24, 48, and 72 h, cell migration was observed. The scratch gap in the CA-V NP group

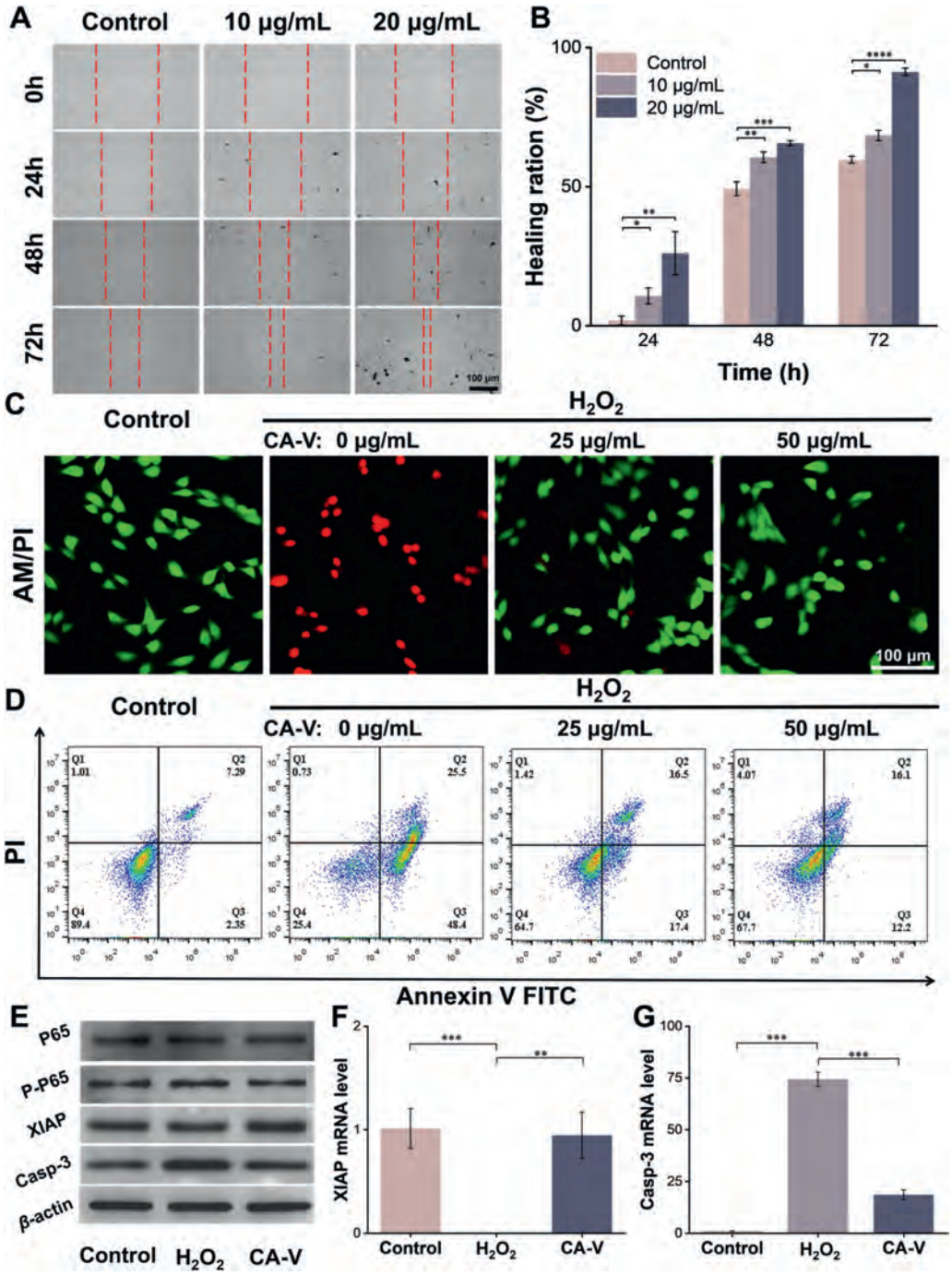

Figure 5 CA-V NPs promote cell migration and inhibit apoptosis. (A) Microscopy images of CA-V NPs promoting L929 cell migration (scale bar = 100 μm). (B) Statistical analysis of the cell migration rate. (C) Confocal fluorescence images of H_2O_2-induced inhibition of HUVEC death by CA-V NPs (scale bar = 100 μm). (D) The extent to which CA-V NPs inhibited HUVEC apoptosis under H_2O_2 induction was detected by flow cytometry. (E) Western blot images of P65, P-P65, XIAP, and Caspase-3 protein expression. (F, G) Relative expression of the *XIAP* and *Caspase*-3 mRNAs. Data are presented as mean ± SD ($n = 3$). *$P < 0.05$, **$P < 0.01$, ***$P < 0.005$ and ****$P < 0.001$.

was smaller than that in the control group, indicating significant cell migration (Fig. 5A). According to the statistical analysis of the cell migration healing rates, CA-V NPs significantly promoted cell migration within 24 h. By 72 h, the cells in the CA-V NP group had almost completely contacted and fused, for a healing rate of up to 91.24% (Fig. 5B).

Excessive production of ROS often mediates oxidative stress in cells, ultimately leading to cell apoptosis. By inducing oxidative stress in HUVECs and staining cells with live/dead dyes, it was found that CA-V NPs could reduce the number of dead cells, and this protective ability was positively correlated with the concentration of CA-V NPs (Fig. 5C). Using a dual-staining apoptosis assay kit to examine HUVECs by flow cytometry, we found that the percentages of early apoptotic cells (2.35% *vs*. 48.4%) and late apoptotic cells (7.29% *vs*. 25.5%) in the H_2O_2 model group increased compared to those in the control group (Fig. 5D). Compared to that in the H_2O_2 model group, the frequency of early and late apoptotic cells in the CA-V NP group was significantly lower, with the CA-V NP (50 μg/mL) group showing a significant decrease in the early apoptotic rate to 12.2% and a decrease in the late apoptotic rate to 16.1%. These findings indicate that CA-V NPs can clear intracellular ROS, thereby protecting cells from oxidative stress-induced damage and alleviating oxidative stress-mediated cell apoptosis. Excessive ROS can activate various inflammatory pathways in cells, and the NF-κB pathway is the most classical oxidative stress pathway and is closely related to oxidative stress status, inflammation, and cell apoptosis. In the present study, the regulation of the cell apoptosis pathway by CA-V NPs during this process was studied by detecting the expression of proteins related to NF-κB p65, phosphorylated NF-κB (p-p65), XIAP, and Caspase-3 in an oxidative stress cell model. Western blot experiments showed (Fig. 5E) that the relative protein expression of p-p65 increased in the H_2O_2 model group, and after CA-V NP treatment, p-p65 protein expression decreased. This may be because CA-V NPs can reduce ROS production, thereby downregulating the phosphorylation of the p65 protein and reducing NF-κB pathway activation. Moreover, compared with that in the control group, the XIAP protein expression in the H_2O_2 model group was relatively lower (Supporting Information Fig. S6), and the caspase-3 protein expression was increased (Supporting Information Fig. S7). After CA-V NP treatment, the XIAP protein was upregulated, and the Caspase-3 protein was downregulated, indicating that CA-V NPs could directly inhibit cell apoptosis during oxidative stress by affecting the expression of XIAP. Additionally, this study detected the mRNA expression of XIAP and Caspase-3. Compared with those in the H_2O_2 model group, the CA-V NPs significantly increased the expression of *XIAP* mRNA (Fig. 5F) and decreased the expression of *Caspase-3* (Fig. 5G), consistent with the protein expression results.

3.5. Mechanism of CA-V NPs in alleviating oxidative stress damage

The mechanism through which CA-V NPs alleviate oxidative stress damage was explored through transcriptome sequencing. Using H_2O_2-treated HUVECs to construct an oxidative stress model, whole-genome expression analysis of the model group and CA-V NP (50 μg/mL) treatment group was conducted (Fig. 6G). The differentially expressed genes (DEGs) were analyzed with the H_2O_2-induced model group as control through clustering analysis to determine the differences in gene expression between the H_2O_2 group and the CA-V NP group (Fig. 6A). In the CA-V NP group, 270 genes were upregulated, and 146 genes were downregulated (Fig. 6B). Gene Ontology (GO) analysis revealed that these DEGs were closely related to cell responses to inflammation and cellular biological regulation processes (Fig. 6C). According to the GO analysis, the downregulated genes included a large number of genes associated with cell apoptosis-related biological processes and signaling pathways (Fig. 6E), consistent with the results of earlier experiments in this study. Kyoto Encyclopedia of Genes and Genomes (KEGG) pathway enrichment analysis (Fig. 6D) revealed that the TNF-α, FoxO, JAK-STAT, IL-17, and NF-κB signaling pathways were closely related to the therapeutic mechanism of CA-V NPs. Furthermore, KEGG enrichment analysis revealed that the genes related to oxidative stress and inflammation whose expression was significantly downregulated were enriched in the TNF-α, FoxO, IL-17, and NF-κB signaling pathways (Fig. 6F). The TNF-α, IL-17, and NF-κB signaling pathways mediate inflammation, and their downregulation can alleviate inflammation and reduce the release of inflammatory mediators. Downregulation of the FoxO and NF-κB signaling pathways can alleviate the induction of oxidative stress. Multiple oxidative stress pathways interact with inflammatory pathways, ultimately playing a collaborative role in inhibiting cell apoptosis.

3.6. In vitro programming of macrophages by CA-V NPs suppresses the inflammatory response

Inflammation is closely associated with oxidative stress, and excessive production of ROS often promotes the activation of inflammatory cells and the release of inflammatory factors. Macrophages play a crucial role in the inflammatory response, and M1-activated macrophages are essential for clearing invading pathogens. However, M1-type macrophages can hinder tissue repair. In the present study, RAW 264.7 cells were costimulated with LPS and IFN-γ to construct an inflammatory cell model (Fig. 7A). In the LPS and IFN-γ induced inflammatory model, immunofluorescence staining of iNOS and CD206 proteins on the surface of M1 and M2 macrophages, respectively, revealed elevated iNOS protein expression and decreased CD206 expression in RAW 264.7 cells stimulated with LPS and IFN-γ compared to those in the control group. Compared to that in the model group, the fluorescence of iNOS on the RAW 264.7 cell surface decreased with increasing concentrations of CA-V NPs, while the CD206 fluorescence increased. These findings suggested that CA-V NPs effectively promoted the transition of RAW 264.7 cells from M1 to M2. Flow cytometry revealed a decrease in the percentage of iNOS-stained cells from 62.5% to 46.1% and an increase in the percentage of CD206-stained cells from 24.9% to 52.7% after CA-V NP treatment, consistent with the results of confocal microscopy (Fig. 7B).

To further understand the expression of inflammatory-related cytokines during this process, ELISAs were conducted. The results showed a significant increase in the proinflammatory factors IL-6 (Fig. 7C) and TNF-α (Fig. 7D) and a decrease in the anti-inflammatory factor IL-10 (Fig. 7E) in the model group compared to those in the control group. After CA-V NP treatment, the expression of IL-6 and TNF-α decreased, while that of IL-10 increased, and these changes were positively correlated with the CA-V NP concentration.

To investigate the mechanism by which CA-V NPs regulate macrophage activation and reduce inflammatory factor expression, this study examined the chemotactic factors of the CXC and CC series. WB (Fig. 7F, Supporting Information Figs. S8 and S9) revealed significant upregulation of the CXCL2 and CCL4

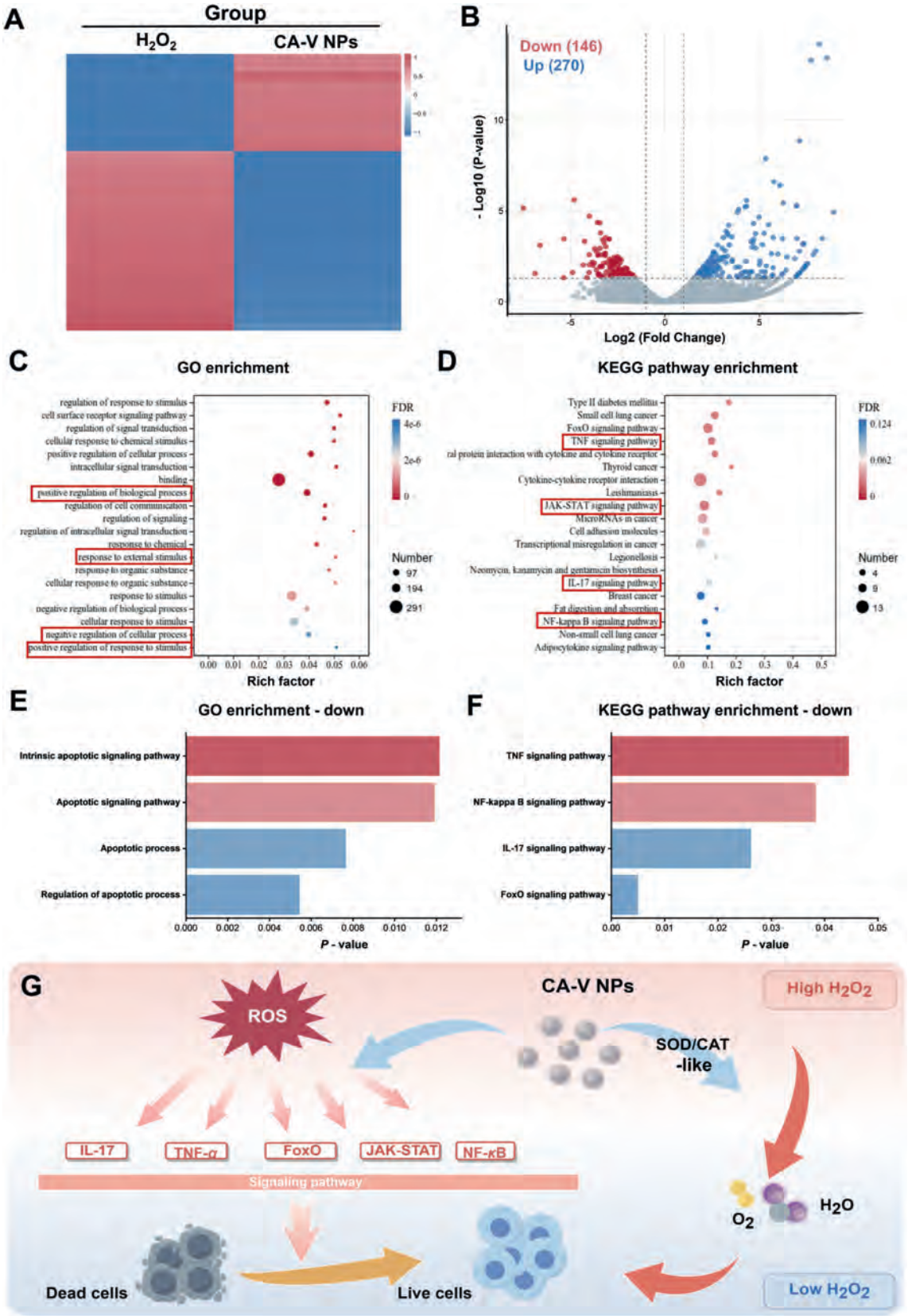

Figure 6 Mechanism by which CA-V NPs alleviate oxidative stress injury. (A) Heatmap of significantly up- and downregulated genes after CA-V NP treatment. (B) Volcano plots of up and down regulated genes after treatment with CA-V NPs. (C) GO enrichment analysis of the DEGs. (D) KEGG enrichment analysis of the DEGs. (E) GO enrichment analysis of DEGs associated with the downregulation of apoptosis. (F) KEGG enrichment analysis of DEGs associated with the downregulation of oxidative stress and inflammation. (G) Diagram showing the mechanism by which CA-V NPs alleviate oxidative stress injury.

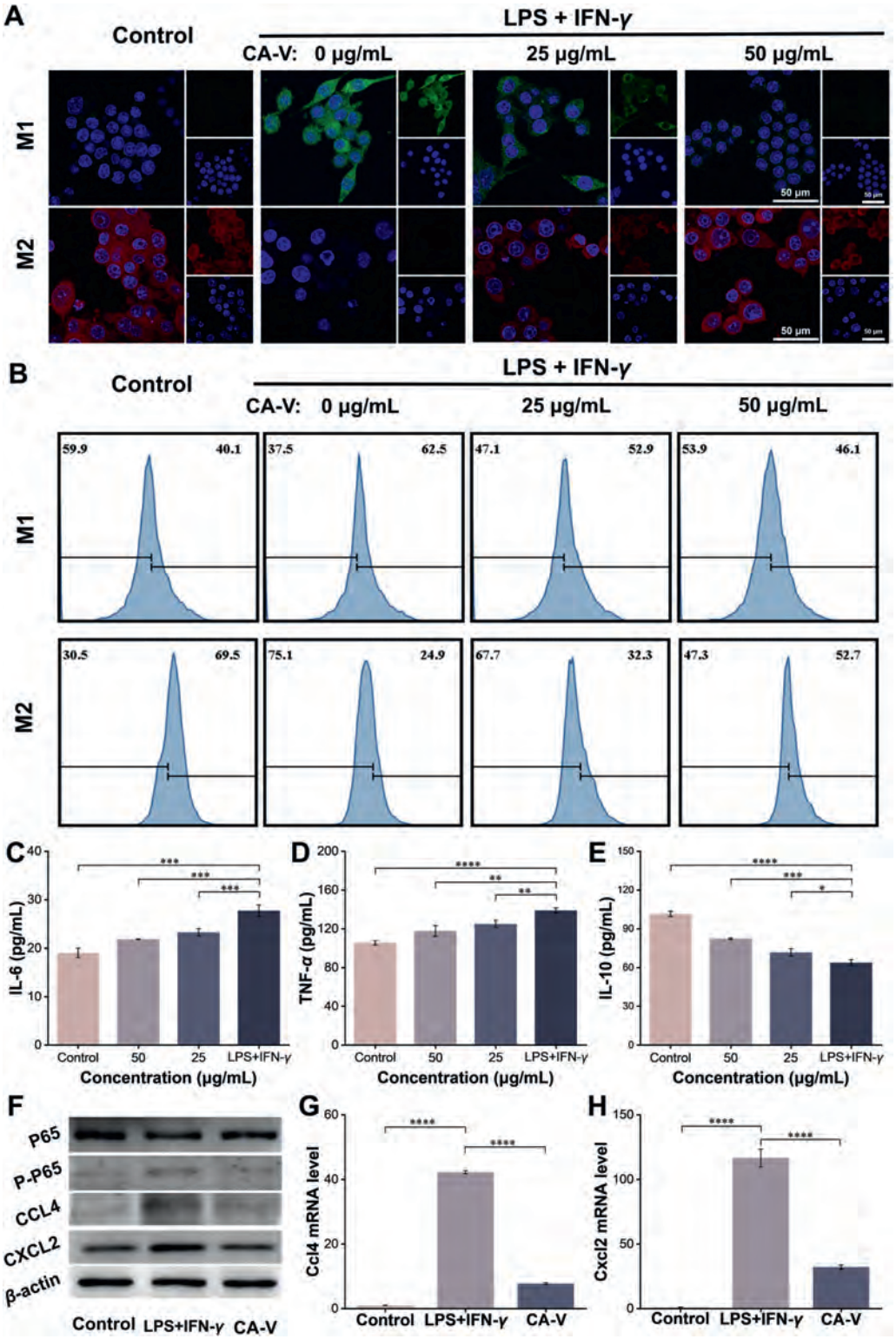

Figure 7 CA-V NPs reprogram macrophages to suppress inflammatory responses. (A) Confocal fluorescence images of CA-V NPs promoting the polarization of RAW 264.7 cells from the M1 type to the M2 type under induction with LPS combined with IFN-γ (scale bar = 50 μm). (B) Flow cytometry assessed the extent to which CA-V NPs promoted the polarization of RAW 264.7 cells from the M1 to the M2 type. (C–E) The expression levels of IL-6, TNF-α, and IL-10 in the supernatant of RAW 264.7 cells were detected *via* ELISA. (F) Western blot images of CCL4 and CXCL2 protein expression. (G–H) Relative expression of the *Ccl4* and *Cxcl2* mRNAs. Data are presented as mean ± SD ($n = 3$). *$P < 0.05$, **$P < 0.01$, ***$P < 0.005$ and ****$P < 0.001$.

proteins in the model group, while CA-V NP treatment led to noticeable downregulation of these proteins. The mRNA expression analysis confirmed the consistent downregulation of *Cxcl2* (Fig. 7G) and *Ccl4* (Fig. 7H) compared to those in the model group. These findings indicate that CA-V NPs can reprogram macrophages at the genetic level and regulate inflammation levels by downregulating proteins and genes associated with macrophage expression.

3.7. Mechanism by which CA-V NPs alleviate the inflammatory response

Similarly, through the use of transcriptome sequencing to explore the mechanism through which CA-V NPs alleviate inflammatory responses, RAW 264.7 cells were induced with LPS and IFN-γ to construct an inflammatory model (Fig. 8E). Differential gene expression analysis was performed between the model group and

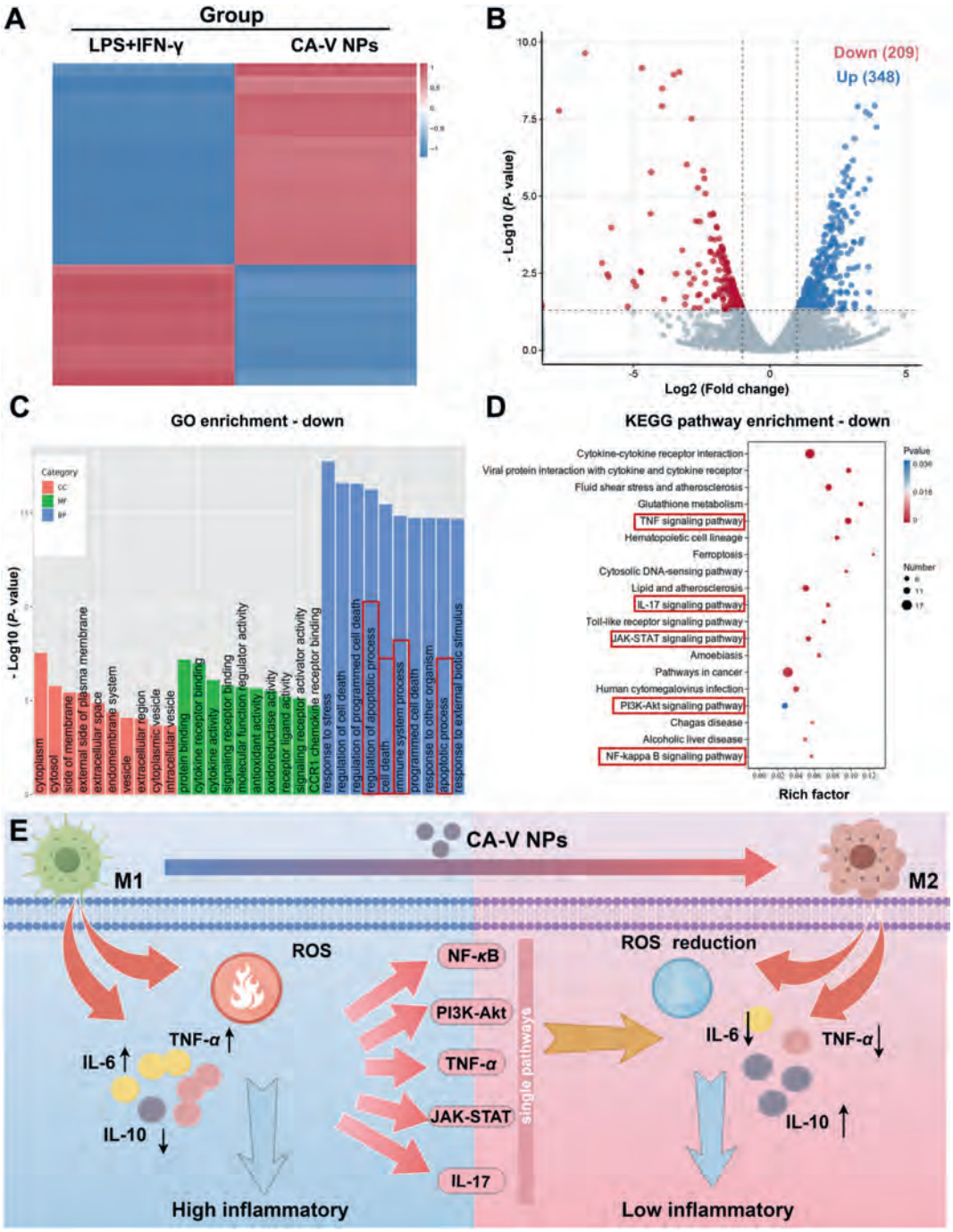

Figure 8 Mechanism by which CA-V NPs reprogram macrophages to suppress the inflammatory response. (A) Heatmap of significantly up- and downregulated genes after CA-V NP treatment. (B) Volcano plots of up- and downregulated genes after treatment with CA-V NPs. (C) GO enrichment analysis of the DEGs (downregulated). (D) KEGG enrichment analysis of the DEGs (downregulated). (E) Diagram of the mechanism by which CA-V NPs reprogram macrophages to inhibit the inflammatory response.

the CA-V NP (50 μg/mL) treatment group. Heatmaps were constructed to show the differences in gene expression between the model and CA-V NP groups (Fig. 8A). A volcano plot revealed 348 upregulated and 209 downregulated genes in the CA-V NP group (Fig. 8B). GO analysis (Fig. 8C) revealed that these DEGs were related to immune processes, cell death, and apoptosis. KEGG pathway enrichment analysis (Fig. 8D) revealed significant decreases in the expression of genes related to inflammation and apoptosis in the TNF-α, PI3K-Akt, JAK-STAT, IL-17, and NF-κB signaling pathways after CA-V NP treatment.

According to the results of gene transcriptome sequencing of H_2O_2-induced oxidative stress and LPS-induced inflammatory models, CA-V NP treatment significantly downregulated genes related to oxidative stress, the inflammatory response, and cell apoptosis. These genes were enriched in the TNF-α, JAK-STAT, IL-17, and NF-κB signaling pathways. These findings suggested that CA-V NPs, by exerting CAT and SOD enzyme activities, clear reactive substances, reduce the activation of the TNF-α, JAK-STAT, IL-17, and NF-κB signaling pathways, alleviate oxidative stress, downregulate inflammatory responses, and inhibit cell apoptosis.

3.8. CA-V NPs promote healing in skin flaps with I/R injury in vivo

To further understand the antioxidative stress capabilities of CA-V NPs, this study conducted experiments using a model of abdominal skin flap I/R injury. During the process of skin flap I/R, the generation of a large amount of ROS exacerbates inflammation within the tissue, often inducing cell apoptosis and necrosis, ultimately leading to impaired tissue healing. In the present study, skin flaps in an I/R injury model were pretreated with CA-V NPs to observe the therapeutic effect of CA-V NPs in promoting the healing of I/R injury in skin flaps and to explore the underlying mechanisms (Fig. 9A). Before constructing the murine abdominal skin flap I/R injury model, CA-V NPs were used for subcutaneous pretreatment to prevent excessive ROS production. To systematically evaluate the ability of CA-V NPs to promote skin flap healing, mice subjected to different treatments were observed, and the healing of skin flaps was recorded on different days. After 48 h of treatment, ROS were detected in the mid-sections of the skin flap tissues in each group, and the levels of inflammatory and anti-inflammatory factors in the tissues were measured *via* ELISA. On Day 7, laser speckle technology and color doppler flow imaging (CDFI) were used to assess the surface blood flow of the skin flaps in each group of mice. Additionally, hematoxylin-eosin (H&E) staining and immunohistochemical staining were performed on the skin flaps to evaluate vascular regeneration, cell apoptosis, and the inflammatory state.

At 48 h after modeling, skin flaps from the midline sections of the mice were stained for ROS, and the results showed that, compared to that in the control group, there was a large amount of ROS fluorescence in the skin of mice subjected to ischemia, and this amount did not improve significantly with saline treatment. However, the intensity of ROS fluorescence in the CA-V NP-treated group was significantly lower than that in the control group, indicating that CA-V NPs can effectively neutralize reactive substances and alleviate oxidative stress during skin flap I/R injury (Fig. 9B). ImageJ software was used for semiquantitative analysis of the fluorescence intensity during ROS staining, confirming the staining results (Fig. 9C). ELISA detection of inflammatory factors in the skin flap tissues of mice in each group showed that, compared to those in the model group, the expression of TNF-α (Fig. 9D) and IL-6 (Fig. 9E) decreased, while the expression of IL-10 (Fig. 9F) increased in the CA-V NP group. These results indicate that CA-V NPs can effectively neutralize the excessive ROS generated during tissue damage, reducing the inflammatory level in the tissue.

By recording the process of skin flap healing (Fig. 9G), it was observed that slight skin ischemia occurred at the edge of the flap in the control group on Day 3. However, on Day 5, the necrotic symptoms improved, and complete healing was achieved without local tissue ischemia or necrosis on Day 7. The skin flaps of mice in the I/R model group and the saline group showed varying degrees of necrosis within 7 days, with a larger necrotic area. In the CA-V NP-treated group, necrosis appeared at the distal end of the skin flap on Day 1, but the necrotic area was smaller than that in the model group and saline group. During the subsequent healing process, the skin flaps in the CA-V NP-treated group gradually healed. On Day 7, the distal skin flap showed minimal ischemia; the distal skin flap healed better than that in the other two groups. On Day 7, blood flow assessment showed that laser speckle technology intuitively reflected the rich blood flow on the surface of the skin flap in the control group and the CA-V NP-treated group, which was far superior to that in the model group and saline group. Color Doppler imaging also showed similar results, with the CA-V NP-treated group having far more blood vessels on the surface of the skin flap than the model group and saline group. Through statistical analysis of the survival rates of different groups of skin flaps at different times, it was found that the survival rates of each group of skin flaps tended to first decrease and then increase (Fig. 9H). On Day 3, the survival rate of the flaps in the CA-V NP treatment group decreased slightly (73.30%) but was much greater than that in the model group (43.51%) and the physiological saline group (46.64%). On Day 7, the survival rate of the skin flaps in the CA-V NP treatment group was 85.59%, which was far greater than that in the model group (55.70%) and the physiological saline group (57.03%).

On Day 7, the skin flaps were subjected to H&E staining, it was observed that the epidermis of the model group and physiological saline group was partially lost, with disrupted subcutaneous structures and almost no sebaceous glands or vascular growth. In contrast, the CA-V NP group exhibited an intact epidermis with distributed sebaceous glands and blood vessels (Fig. 10A). Quantitative analysis of the number of blood vessels (Fig. 10B) and hair follicles (Fig. 10C) in each group revealed that the number of blood vessels in the CA-V NP group was significantly greater than that in the other model groups and the physiological saline group. To further observe vascular formation, CD31 immunohistochemical staining was performed on the skin flaps. Semiquantitative analysis of the results (Fig. 10D) revealed that the CD31 concentration in the CA-V NP group was much greater than that in the model group and physiological saline group, consistent with the laser speckle and blood flow Doppler results. CD68, a marker of macrophages and a crucial indicator of tissue inflammation was downregulated in the CA-V NP group (Fig. 10E), indicating that pretreatment with CA-V NPs effectively reduced the inflammatory level in the skin flap, confirming the earlier ELISA results. Additionally, immunohistochemical staining for CXCL2, CCL4, XIAP, and Caspase-3 was

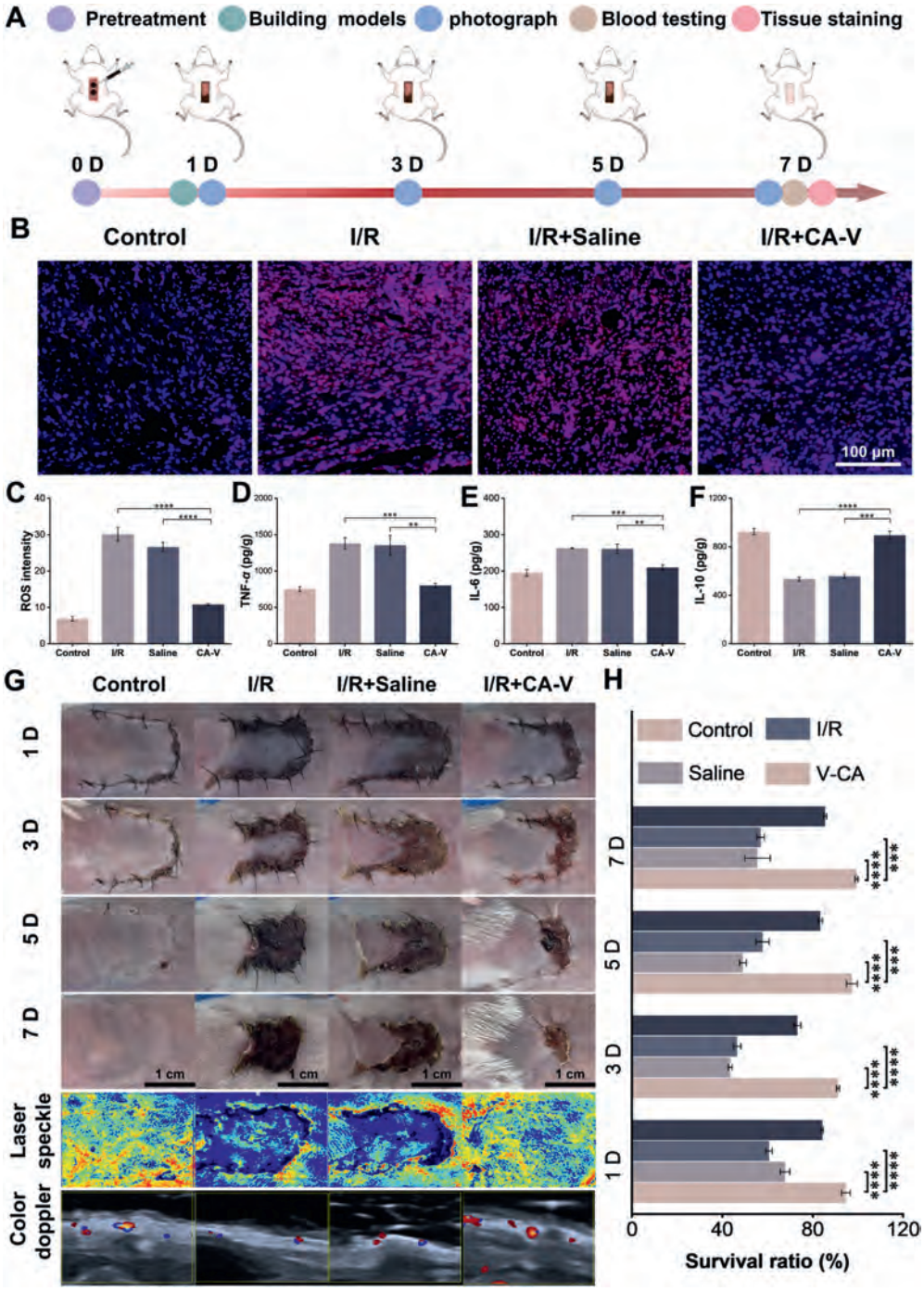

Figure 9 CA-V NPs promote the healing of skin flap I/R injury *in vivo*. (A) Schematic diagram of CA-V NPs in the treatment of mouse flap I/R injury. (B) ROS staining of skin flaps in each group after 48 h of treatment (scale bar = 100 μm). (C) Semiquantification of ROS staining in skin flaps from each group. (D–F) ELISA for the expression levels of IL-6, TNF-α, and IL-10 in the mid-section skin flap tissues at the 48 h of treatment. (G) Photographs of flaps after different treatments were obtained on Days 1, 3, 5, and 7, and the laser speckle and color doppler were used to assess flap surface perfusion on Day 7 (scale bar = 1 cm). (H) Statistical analysis of flap survival ratio. Data are presented as mean ± SD ($n = 3$). $^{**}P < 0.01$, $^{***}P < 0.005$ and $^{****}P < 0.001$.

performed at the junction of the skin flap. The levels of CXCL2 (Fig. 10F) and CCL4 (Fig. 10G) in the CA-V NP group were lower than those in the model group and physiological saline group, consistent with the CD68 staining results and cell experiments. A reduction in macrophages also decreased the release of CXCL2 and CCL4, simultaneously inhibiting macrophage activation and leading to positive regulation of the inflammatory response. In particular, the XIAP level in the CA-V NP group increased (Fig. 10H), while the Caspase-3 level decreased (Fig. 10I), indicating an effective reduction in cellular apoptosis, closely associated with the

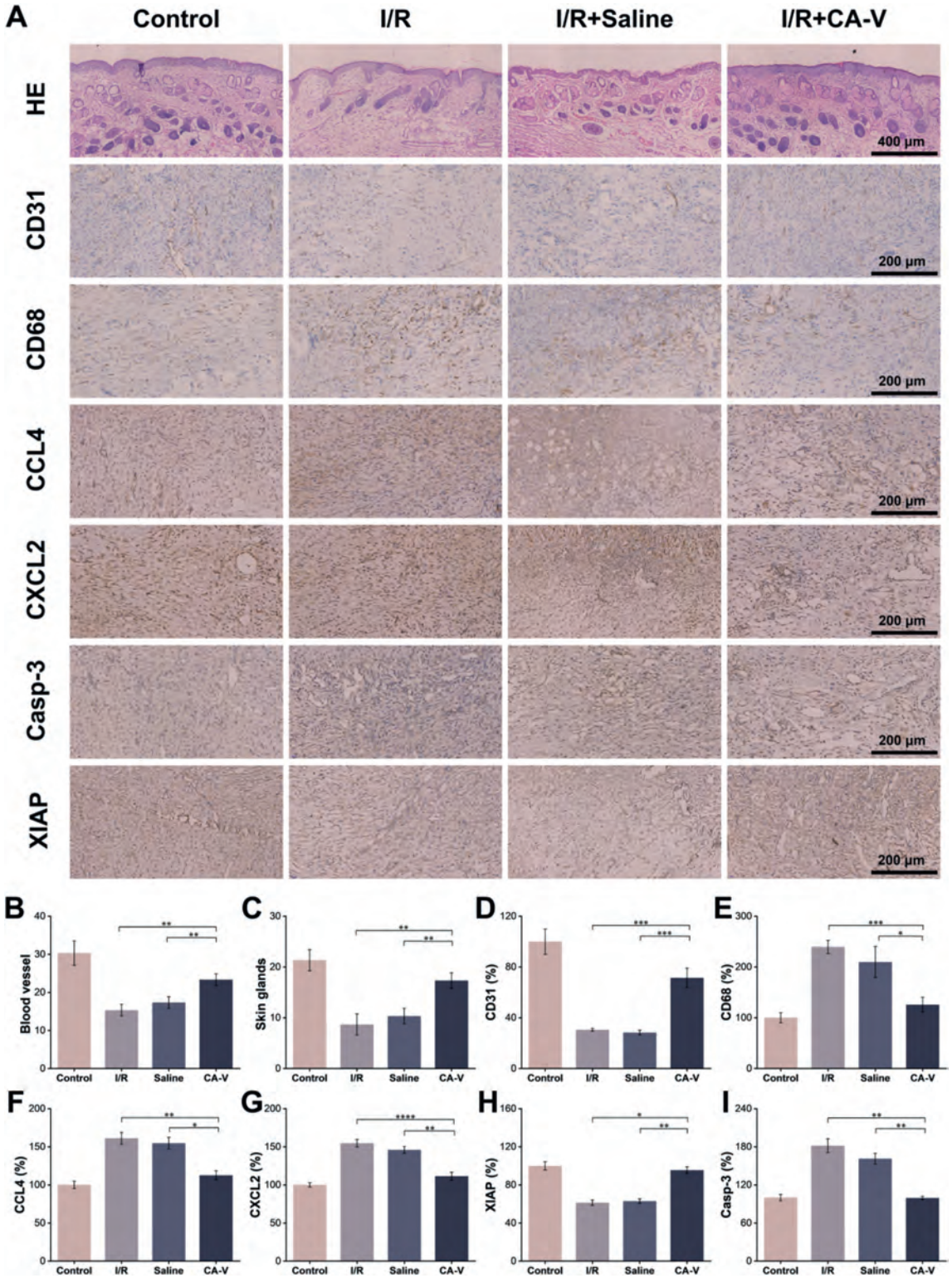

Figure 10 Evaluation of the ability of CA-V NPs to promote skin flap healing *in vivo*. (A) Images of H&E staining and immunohistochemical staining for CD31, CD68, CCL4, CXCL2, XIAP, and Caspase-3 in mid-section flap tissue sections on Day 7. (B, C) Statistical analysis of the number of blood vessels and glands in HE-stained skin flap tissue sections. (D−I) Semiquantitative analysis of immunohistochemical staining of tissue sections. Data are presented as mean ± SD ($n = 3$). *$P < 0.05$, **$P < 0.01$, ***$P < 0.005$ and ****$P < 0.001$.

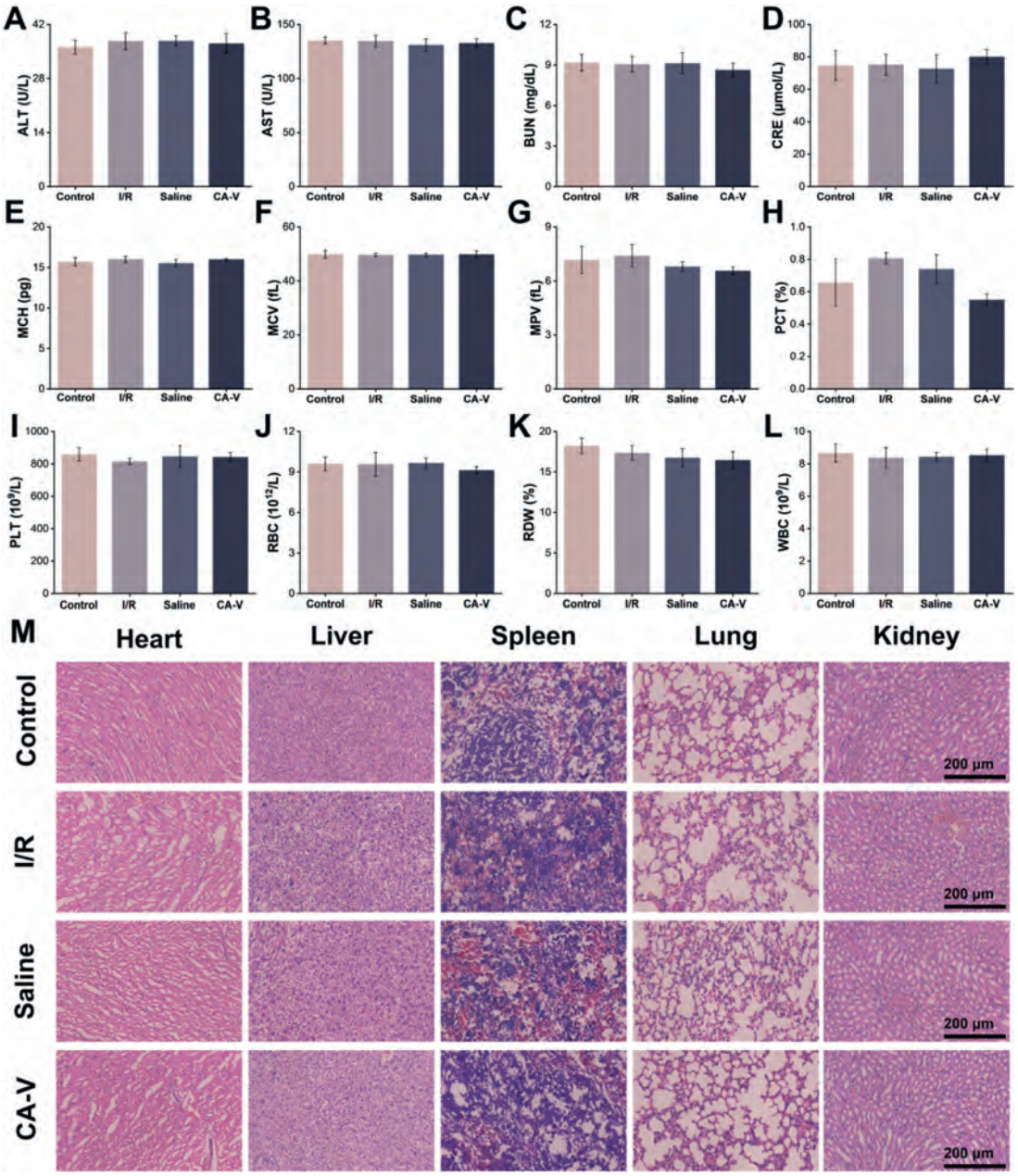

Figure 11 *In vivo* biocompatibility assessment of CA-V NPs. (A−L) Blood parameters and biochemical indices of mice in different groups on Day 7. (M) Images of H&E-stained sections of major organs (heart, liver, spleen, lungs, and kidneys) from the different groups of mice on Day 7. Data are presented as mean ± SD ($n = 3$).

downregulation of oxidative stress and the inflammatory response. The results of these animal experiments suggest that CA-V NPs reduce the necrosis rate of I/R-damaged flaps by improving vascular formation and alleviating the inflammatory response.

Finally, from an *in vivo* experimental perspective, further evaluation of the biocompatibility of the CA-V NPs was conducted. On Day 7, blood indices of mice from each group were tested, and major organs (heart, liver, spleen, lung, and kidney) were subjected to H&E staining. Blood index testing revealed no significant differences in routine blood test results or biochemical parameters among the groups (Fig. 11A-L). The staining results of major organs showed no differences in tissue morphology between the groups, indicating that CA-V NPs had no significant toxic effects on the mice (Fig. 11M).

4. Conclusions

This study successfully prepared uniformly sized and structurally stable ultrasmall metal polyphenol nanoparticles (CA-V NPs). These nanoparticles exhibited outstanding reactive substance clearance capabilities and dual activities similar to those of SOD and CAT, effectively alleviating intracellular oxidative stress while supplying O_2 to cells. *In Vitro* experiments demonstrated that CA-

V NPs suppressed cell apoptosis by modulating the XIAP/Caspase-3 pathway in HUVECs and reprogrammed macrophages by downregulating the chemotactic factors CCL4 and CXCL2. Sequencing revealed that CA-V NPs activated multiple signaling pathways, including the TNF-α, JAK-STAT, IL-17, and NF-κB pathways, leading to the downregulation of genes associated with inflammation and oxidative stress. This effectively alleviated H_2O_2-induced cellular oxidative stress, reduced LPS- and IFN-γ-induced inflammation, and inhibited cell apoptosis. Animal experiments demonstrated that CA-V NPs could alleviate early reperfusion oxidative stress, reduce cell damage during I/R injury of skin flaps, and improve flap survival rates. Therefore, CA-V NPs could emerge as a novel therapeutic strategy for I/R injury of skin flaps by clearing ROS and inhibiting inflammation and apoptosis. Additionally, CA-V NPs have opened up new treatment targets, such as XIAP, CCL4, and CXCL2, for I/R injury of skin flaps.

Acknowledgments

This work was supported by the National Natural Science Foundation of China (Grant Nos. 82172204, 82372552 and 82372517), the Anhui Key Research and Development Plan (Grant No. 202104j07020027, China), the Excellent Youth of Natural Science Research Projects in Anhui Province Universities (2023AH030060), the Basic and Clinical Cooperative Research and Promotion Program of Anhui Medical University (No. 2021xkjT028, China), the Research Fund of Anhui Institute of Translational Medicine (2022zhyx-C01, China), and the Scientific Research Programme for Higher Education Institutions in Anhui Province (2023AH040371, China). The authors would like to thank the Shiyanjia Laboratory (www.shiyanjia.com) for the XPS test. The authors would like to thank for the drawing of Figs. 6G and 8E.

Author contribution

Xinyu Zhao: Writing − original draft, Visualization, Validation, Software, Resources, Methodology, Investigation, Formal analysis, Data curation, Conceptualization. Jie Shan: Visualization, Validation, Methodology, Data curation, Conceptualization. Hanying Qian: Validation, Software, Methodology, Investigation, Formal analysis, Data curation, Conceptualization. Xu Jin: Visualization, Software, Formal analysis, Data curation, Conceptualization. Yiwei Sun: Software, Methodology, Formal analysis. Jianghao Xing: Software, Formal analysis, Data curation. Qingrong Li: Visualization, Software, Methodology. Xu-Lin Chen: Writing − review & editing, Visualization, Supervision, Resources, Methodology, Investigation, Funding acquisition, Formal analysis, Data curation, Conceptualization. Xianwen Wang: Writing − review & editing, Visualization, Validation, Supervision, Software, Resources, Project administration, Methodology, Investigation, Funding acquisition, Formal analysis, Data curation, Conceptualization.

Conflicts of interest

The authors have no conflicts of interest to declare.

Appendix A. Supporting information

Supporting information to this article can be found online at https://doi.org/10.1016/j.apsb.2024.08.022.

References

1. Ballestín A, Casado JG, Abellán E, Vela FJ, Álvarez V, Usón A, et al. Ischemia-reperfusion injury in a rat microvascular skin free flap model: a histological, genetic, and blood flow study. *Plos One* 2018; **13**:e0209624.
2. Lum H, Barr DA, Shaffer JR, Gordon RJ, Ezrin AM, Malik AB. Reoxygenation of endothelial cells increases permeability by oxidant-dependent mechanisms. *Circ Res* 1992;**70**:991−8.
3. Siemionow M, Arslan E. Ischemia/reperfusion injury: a review in relation to free tissue transfers. *Microsurg* 2004;**24**:468−75.
4. Winterbourn CC. Reconciling the chemistry and biology of reactive oxygen species. *Nat Chem Biol* 2008;**4**:278−86.
5. Xu SB, Chang LN, Zhao XJ, Hu YA, Lin YY, Chen ZH, et al. Preparation of epigallocatechin gallate decorated Au-Ag nano-heterostructures as NIR-sensitive nano-enzymes for the treatment of osteoarthritis through mitochondrial repair and cartilage protection. *Acta Biomater* 2022;**144**: 168−82.
6. Li X, Han Z, Wang T, Ma C, Li H, Lei H, et al. Cerium oxide nanoparticles with antioxidative neurorestoration for ischemic stroke. *Biomaterials* 2022;**291**:121904.
7. Sinha K, Das J, Pal PB, Sil PC. Oxidative stress: the mitochondria-dependent and mitochondria-independent pathways of apoptosis. *Arch Toxicol* 2013;**87**:1157−80.
8. Dunnill C, Patton T, Brennan J, Barrett J, Dryden M, Cooke J, et al. Reactive oxygen species (ROS) and wound healing: the functional role of ROS and emerging ROS-modulating technologies for augmentation of the healing process. *Int Wound J* 2017;**14**:89−96.
9. Yang BW, Chen Y, Shi JL. Reactive oxygen species (ROS)-based nanomedicine. *Chem Rev* 2019;**119**:4881−985.
10. Wang ZR, Zhang RF, Yan XY, Fan KL. Structure and activity of nanozymes: inspirations for de novo design of nanozymes. *Mater Today* 2020;**41**:81−119.
11. Wu JJX, Wang XY, Wang Q, Lou ZP, Li SR, Zhu YY, et al. Nanomaterials with enzyme-like characteristics (nanozymes): next-generation artificial enzymes (II). *Chem Soc Rev* 2019;**48**:1004−76.
12. Lee J, Liao H, Wang Q, Han J, Han JH, Shin HE, et al. Exploration of nanozymes in viral diagnosis and therapy. *Exploration* 2022;**2**:20210086.
13. Zandieh M, Griffiths E, Waldie A, Li S, Honek J, Rezanezhad F, et al. Catalytic and biocatalytic degradation of microplastics. *Exploration* 2023:20230018.
14. Singh N, Savanur MA, Srivastava S, D'Silva P, Mugesh G. A redox modulatory Mn_3O_4 nanozyme with multi-enzyme activity provides efficient cytoprotection to human cells in a Parkinson's disease model. *Angew Chem Int Edit* 2017;**56**:14267−71.
15. Zhang C, Li QR, Shan J, Xing JH, Liu XY, Ma Y, et al. Multifunctional two-dimensional Bi_2Se_3 nanodiscs for anti-inflammatory therapy of inflammatory bowel diseases. *Acta Biomater* 2023;**160**:252−64.
16. Weng Q, Sun H, Fang C, Xia F, Liao H, Lee J, et al. Catalytic activity tunable ceria nanoparticles prevent chemotherapy-induced acute kidney injury without interference with chemotherapeutics. *Nat Commun* 2021; **12**:1436.
17. Zhao HQ, Zhang RF, Yan XY, Fan KL. Superoxide dismutase nanozymes: an emerging star for anti-oxidation. *J Mater Chem B* 2021;**9**:6939−57.
18. Kwon K, Jung J, Sahu A, Tae G. Nanoreactor for cascade reaction between SOD and CAT and its tissue regeneration effect. *J Control Release* 2022;**344**:160−72.

19. Li J, Song J, Deng Z, Yang J, Wang X, Gao B, et al. Robust reactive oxygen species modulator hitchhiking yeast microcapsules for colitis alleviation by trilogically intestinal microenvironment renovation. *Bioact Mater* 2024;**36**:203−20.
20. Li Q, Dong M, Han Q, Zhang Y, Yang D, Wei D, et al. Enhancing diabetic wound healing with a pH-responsive nanozyme hydrogel featuring multi-enzyme-like activities and oxygen self-supply. *J Control Release* 2023;**365**:905−18.
21. Deng Z, Ma W, Ding C, Wei C, Gao B, Zhu Y, et al. Metal polyphenol network/cerium oxide artificial enzymes therapeutic nanoplatform for MRI/CT-aided intestinal inflammation management. *Nano Today* 2023; **53**:102044.
22. Xu D, Wu L, Yao H, Zhao L. Catalase-like nanozymes: classification, catalytic mechanisms, and their applications. *Small* 2022;**18**:2203400.
23. Jin X, Zhang W, Shan J, He J, Qian H, Chen X, et al. Thermosensitive hydrogel loaded with nickel-copper bimetallic hollow nanospheres with SOD and CAT enzymatic-Like activity promotes acute wound healing. *ACS Appl Mater Inter* 2022;**14**:50677−91.
24. Ye YY, Yu HL, Chen BH, Zhao YF, Lv B, Xue GH, et al. Engineering nanoenzymes integrating Iron-based metal organic frameworks with Pt nanoparticles for enhanced photodynamic-ferroptosis therapy. *J Colloid Interf Sci* 2023;**645**:882−94.
25. Liang MM, Yan XY. Nanozymes: from new concepts, mechanisms, and standards to applications. *Acc Chem Res* 2019;**52**:2190−200.
26. Feng W, Han X, Hu H, Chang M, Ding L, Xiang H, et al. 2D vanadium carbide MXenzyme to alleviate ROS-mediated inflammatory and neurodegenerative diseases. *Nat Commun* 2021;**12**:2203.
27. Amaral LM, Moniz T, Silva AM, Rangel M. Vanadium compounds with antidiabetic potential. *Int J Mol Sci* 2023;**24**:15675.
28. Ghalichi F, Ostadrahimi A, SaghafiAsl M. Vanadium and diabetic dyslipidemia: a systematic review of animal studies. *J Trace Elem Med Bio* 2022;**71**:126955.
29. Zhao X, Liu Z, Liu H, Guo J, Long S. Hybrid molecules based on caffeic acid as potential therapeutics: a focused review. *Eur J Med Chem* 2022;**243**:114745.
30. Chiang YF, Lin IC, Huang KC, Chen HY, Ali M, Huang YJ, et al. Caffeic acid's role in mitigating polycystic ovary syndrome by countering apoptosis and ER stress triggered by oxidative stress. *Biomed Pharmacother* 2023;**166**:115327.
31. Fratantonio D, Speciale A, Canali R, Natarelli L, Ferrari D, Saija A, et al. Low nanomolar caffeic acid attenuates high glucose-induced endothelial dysfunction in primary human umbilical-vein endothelial cells by affecting NF-κB and Nrf2 pathways. *Biofactors* 2017;**43**:54−62.
32. Lee ES, Park SH, Kim MS, Han SY, Kim HS, Kang YH. Caffeic acid disturbs monocyte adhesion onto cultured endothelial cells stimulated by adipokine resistin. *J Agr Food Chem* 2012;**60**:2730−9.
33. Pérez R, Burgos V, Marín V, Camins A, Olloquequi J, González Chavarría I, et al. Caffeic acid phenethyl ester (CAPE): biosynthesis, derivatives and formulations with neuroprotective activities. *Antioxidants* 2023;**12**:1500.
34. Yu Cm, Wang Y, Ren Sc, Liu Zl, Zhu Cl, Liu Q, et al. Caffeic acid modulates activation of neutrophils and attenuates sepsis-induced organ injury by inhibiting 5-LOX/LTB4 pathway. *Int Immunopharmacol* 2023;**125**:111143.
35. Hassan NA, El Bassossy HM, Mahmoud MF, Fahmy A. Caffeic acid phenethyl ester, a 5-lipoxygenase enzyme inhibitor, alleviates diabetic atherosclerotic manifestations: effect on vascular reactivity and stiffness. *Chem-Biol Interact* 2014;**213**:28−36.
36. Zielińska D, Zieliński H, Laparra Llopis JM, Szawara Nowak D, Honke J, Giménez Bastida JA. Caffeic acid modulates processes associated with intestinal inflammation. *Nutrients* 2021;**13**:554.
37. Castro MFV, Stefanello N, Assmann CE, Baldissarelli J, Bagatini MD, da Silva AD, et al. Modulatory effects of caffeic acid on purinergic and cholinergic systems and oxi-inflammatory parameters of streptozotocin-induced diabetic rats. *Life Sci* 2021;**277**:119421.
38. Matowane GR, Mashele SS, Makhafola TJ, Chukwuma CI. The ameliorative effect of zinc acetate with caffeic acid in the animal model of type 2 diabetes. *Biomed Pharmacother* 2023;**163**: 114779.
39. Zhang Y, Wu Q, Zhang L, Wang Q, Yang Z, Liu J, et al. Caffeic acid reduces A53T α-synuclein by activating JNK/Bcl-2-mediated autophagy in vitro and improves behaviour and protects dopaminergic neurons in a mouse model of Parkinson's disease. *Pharmacol Res* 2019;**150**:104538.
40. Brautigan DL, Gielata M, Heo J, Kubicka E, Wilkins LR. Selective toxicity of caffeic acid in hepatocellular carcinoma cells. *Biochem Bioph Res Co* 2018;**505**:612−7.
41. Saavedra MJ, Borges A, Dias C, Aires A, Bennett RN, Rosa ES, et al. Antimicrobial activity of phenolics and glucosinolate hydrolysis products and their synergy with streptomycin against pathogenic bacteria. *Med Chem* 2010;**6**:174−83.
42. Sivakumar S, Girija ASS, Priyadharsini JV. Evaluation of the inhibitory effect of caffeic acid and gallic acid on tetR and tetM efflux pumps mediating tetracycline resistance in Streptococcus sp., using computational approach. *J King Saud Univ Sci* 2020;**32**:904−9.
43. Mude H, Maroju PA, Balapure A, Ganesan R, Dutta JR. Water-soluble caffeic acid-dopamine acid-base complex exhibits enhanced bactericidal, antioxidant, and anticancer properties. *Food Chem* 2022;**374**: 131830.
44. Hou R, Lu TX, Gao W, Shen J, Yu ZY, Li DT, et al. Prussian blue nanozyme promotes the survival rate of skin flaps by maintaining a normal microenvironment. *Acs Nano* 2022;**16**:9559−71.